

Critical Influence of the Pattern of Tropical Ocean Warming on Remote Climate Trends

Sang-Ik Shin • Prashant D. Sardeshmukh

Sang-Ik Shin (✉) • Prashant D. Sardeshmukh
CIRES Climate Diagnostics Center, University of Colorado and NOAA Earth System Research
Laboratory,
R/PSD1, 325 Broad Way,
Boulder, CO 80305-3328, USA
E-mail: sangik.shin@noaa.gov
Tel.: +1-303-497-4424
Fax: +1-303-497-6449

Abstract

Evidence is presented that the recent trend patterns of surface air temperature and precipitation over the land masses surrounding the North Atlantic ocean (North America, Greenland, Europe, and North Africa) have been strongly influenced by the warming pattern of the tropical oceans. The current generation of atmosphere-ocean coupled climate models with prescribed radiative forcing changes generally do not capture these regional trend patterns. On the other hand, even uncoupled atmospheric models without the prescribed radiative forcing changes, but with the observed oceanic warming specified only in the tropics, are more successful in this regard. The tropical oceanic warming pattern is poorly represented in the coupled simulations. This error needs to be reduced to increase confidence in regional climate change projections around the globe.

1 Introduction

Climate models are now sufficiently advanced that they can reasonably simulate the global mean as well as some continental-scale aspects of recent climate change, and provide important guidance on future changes on these scales in response to anthropogenic changes in radiative forcing (IPCC 2007). This has led to increased interest in model skill in simulating and predicting the changes on even smaller sub-continental scales, that could be different and more severe than the global mean or continental-scale changes (IPCC 2007; Sidall and Kaplan 2008; Ray et al. 2008). To this end we have compared multi-model ensemble simulations of the last half-century with corresponding observations, focusing on the land masses around the North Atlantic Ocean – North America, Greenland, Europe, and North Africa. We chose these regions partly for their relatively better observational data coverage, and partly because they lie within the domains of influence of important natural climate phenomena such as the El Niño Southern Oscillation (ENSO), the Pacific Decadal Oscillation (PDO), the North Atlantic Oscillation (NAO), the Arctic Oscillation (AO), and the Atlantic Multi-decadal Oscillation (AMO).

Our original motivation was to clarify the relative importance of the external versus internal trend generation mechanisms over these regions. Previous studies had suggested important roles for external radiative forcing changes due to CO₂ increases (Folland et al. 1998, Bracco et al. 2004; Deser and Phillips 2009), regional and remote sea surface temperature (SST) changes (Graham 1994; Rodwell et al. 1999; Hoerling et al. 2001; Sutton and Hodson 2003; Schneider et al. 2003; Deser et al. 2004; Hurrell et al. 2004;

Deser and Phillips 2009), as well as natural atmospheric variability over the North Atlantic and European sectors (Schneider et al. 2003; Bracco et al. 2004; Hurrell et al. 2004). We were especially interested in clarifying the role of the SST changes, which if important would highlight the importance of correctly representing those changes in climate models to capture the trends over these land areas. Also, Compo and Sardeshmukh (2009) had recently demonstrated the substantial influence even in a radiatively warming world of global SST trends on continental temperature trends. We were interested in determining to what extent their conclusion applied to our "Atlantic Rim" land masses of relatively large natural variability, to not just surface air temperature but also precipitation, and to what degree the changes in the tropical SSTs dominated this SST influence.

The important role of SST variations in interannual and longer timescale climate variability is very well recognized. Numerous studies have shown that many aspects of observed climate variations around the globe can be captured in uncoupled atmospheric general circulation model (GCM) simulations in which the time history of the observed global SSTs is prescribed as lower boundary conditions (e.g. Gates 1992; Lau 1997). Indeed the progress in seasonal to interannual predictions is mainly attributable to this recognition of the role of SSTs (Goddard et al. 2001; Barnston et al. 2005). It has also been shown that many aspects of the response to global SST changes can be reproduced in simulations in which the SST changes are prescribed only in the tropics (e.g. Lau and Nath 1994; Lau 1997; Saravanan 1998; Graham 1994; Hoerling et al. 2001; Hoerling and Kumar 2003; Schneider et al. 2003; Deser et al. 2004; Hurrell et al. 2004; Schubert et al.

2004, Herweijer and Seager 2008, and many others). On interannual time scales, most but not all of these tropical SST changes are associated with ENSO, a natural oscillation of the tropical climate system.

On longer than interannual time scales, the radiatively forced component of climate variations becomes progressively more important. Even on these longer time scales, however, the correct representation of SST changes remains important for representing changes over land, because the radiatively forced components of the SST changes can, depending on their magnitude, strongly impact the changes over land. Indeed several studies have suggested that such an indirect land response to radiative forcing through the SST response (that one may loosely call an ‘SST feedback’) is much larger than the direct land response to radiative forcing (Folland et al 1998, Schneider et al 2003, Bracco et al 2004, Compo and Sardeshmukh 2009, Hoerling et al 2009, Deser and Phillips 2009).

Our own analysis here provides additional strong evidence that the spatial *patterns* of the SST variations on these longer time scales have an important influence on the spatial patterns of the trends even in regions remote from the SST forcing. Specifically, we show that the spatial patterns of the surface air temperature and precipitation trends in the second half of the 20th century over our Atlantic Rim land masses were strongly influenced by the pattern of the tropical SST warming trend over the same period. This conclusion is derived from two separate sets of model simulations. One set, generated using the same coupled atmosphere-ocean climate models used in the Fourth Assessment Report (AR4) of the Intergovernmental Panel on Climate Change (IPCC), uses prescribed

observed radiative forcing changes. The other set, generated using uncoupled atmospheric GCMs, uses observed time-varying SSTs prescribed either globally or only in the tropics as lower boundary conditions, but (with a few exceptions noted below) no explicitly specified radiative forcing changes. We first show that the uncoupled simulations are generally better than the coupled simulations at capturing both the patterns and magnitudes of the observed trends over our Atlantic Rim land masses of interest in the second half of the 20th century, and that this better realism is obtained even in simulations in which the observed SSTs are prescribed only in the tropics. We then show that the spatial variation of the observed tropical SST trend field is not well represented in the coupled simulations, even though the tropically averaged SST trend is very well represented. Our analysis thus points to errors in representing the *pattern* of the tropical SST trend as a major source of uncertainty in representing remote climate changes, and raises the hope that reducing such errors will reduce the uncertainty in regional climate predictions around the globe.

2 Model simulations analyzed

We used all available coupled model simulations of the period 1951-1999 from 18 international modeling centers, generated as part of the IPCC's 20th century climate simulations with prescribed time-varying radiative forcings associated with greenhouse gases, aerosols, and solar variations. We also used additional sets of uncoupled atmosphere-only model simulations from 4 modeling centers, with prescribed observed histories of either global or tropical SSTs over this period. We thus used 163 simulations in all: 76 coupled simulations (CPL; Table 1), 66 uncoupled simulations with prescribed

global SST changes (GLB; Table 2), and 21 uncoupled simulations with the SST changes prescribed only in the tropics (TRP; Table 3). In the TRP runs the long-term mean annual cycle of SSTs was prescribed outside the tropics. The 66 uncoupled GLB simulations included 10 simulations with prescribed time-varying radiative forcings in addition to the prescribed time-varying observed SSTs. We did this mainly to reduce sampling uncertainty, given the evidence from previous studies (e.g., Compo and Sardeshmukh 2009) that the direct effect of the radiative forcings in such runs (as opposed to their indirect effect through the SSTs) is minor on the variables considered here.

As climate change indicators over our land masses of interest (in the region 20° to 75°N, 170°W to 40°E), we chose precipitation and near-surface (2-meter) air temperature, not only for their intrinsic importance but also for their impact on simple measures of drought such as the Palmer Drought Severity Index (PDSI; Palmer 1965). We restricted our focus to the changes over land, both because of the better availability of observations over land, and to perform fair comparisons of the coupled simulations with the uncoupled simulations in which the observed boundary conditions (i.e. the SSTs) were prescribed over the oceans, but not over land.

3 Observed and simulated regional climate trends

The observed 50-year trends of annual-mean surface air temperature and precipitation over our land masses of interest are shown in Fig. 1. The temperature trends were derived from an unweighted average of observations compiled at the University of East Anglia Climate Research Unit (UEA-CRU; Mitchell and Jones 2005), the National Aeronautics

and Space Administration's Goddard Institute for Space Studies (NASA-GISS; Hansen et al. 2001), and the National Oceanic and Atmospheric Administration (NOAA; Smith and Reynolds 2005). The precipitation trends were derived from an unweighted average of observations compiled at UEA-CRU (Mitchell and Jones 2005), the Global Precipitation Climatology Centre (GPCC; Rudolf et al. 2005), and NOAA (Chen et al. 2002). These observational temperature and precipitation trend maps may be compared directly with similar maps in Fig. 1 derived from the grand ensemble mean of the 76 coupled simulations, and also the grand ensemble mean of the 87 uncoupled prescribed-SST simulations. The coupled simulations show relatively uniform warming and rather weak precipitation trends that differ substantially from the observed trends. For example, the observed cooling and moistening trends over large parts of the United States are not well simulated, and the observed drying trend over tropical Africa is greatly underestimated. These deficiencies are notably smaller in the uncoupled simulations with prescribed observed SSTs, suggesting a major influence of those SSTs on the trends over these land areas.

A quantitative comparison of the air temperature and precipitation trend fields obtained from each of the 163 simulations with the corresponding observed trend fields is provided in Fig. 2a, using the format of the so-called Taylor diagram (Taylor 2001). Each point on a Taylor diagram depicts the normalized dot product and normalized magnitude of a vector (in our case, the vector of simulated trends over all land points in our domain of interest) with respect to a reference vector (i.e., the corresponding observed trend vector). The normalized dot product may also be identified with the spatial pattern

correlation r , and the normalized magnitude with the root-mean-square (r.m.s.) magnitude ratio A , of the simulated and observed trend fields over the land points in our domain. Note that to focus on the spatially varying parts of the trend fields, we removed the land-averaged trends from both the simulated and observed trend fields before computing these pattern correlations and r.m.s. magnitudes.

In general, the Taylor diagrams show poor pattern correlations and r.m.s. magnitudes of the simulated trend fields relative to the observed fields. Given that the climate system is chaotic, such a poor correspondence would suggest, even if the models were "perfect" (i.e., if there were no errors in model formulation but a large sensitivity of the model integrations to initial conditions) a substantial unpredictable climate noise contribution to the observed trends over this 50-year interval. The Taylor diagrams also show an overall tendency of the trends in the prescribed-SST simulations to compare better with observations than the trends in the coupled simulations, suggesting that a significant portion of the errors in the latter are associated with errors in simulating the observed SSTs. Note that the SST errors are zero in the prescribed-SST simulations by experimental design.

An important point to keep in mind concerning Taylor diagrams is that although they are convenient for comparing a large number of vectors (in our case, 163 simulated trend vectors) with a *single* reference vector (the observed trend vector), they do not accurately show how those vectors compare among themselves, particularly with respect to dot products (i.e. pattern correlations). Such intercomparisons are useful for many purposes.

In our case, they would provide valuable information on the internal consistency of the simulated trends. One straightforward but cumbersome way to gauge this internal consistency would be through construction of 163 separate Taylor diagrams that treat in turn each of the simulated trend vectors as the reference vector. We present instead in Figs. 2b and 2c an alternative and more compact depiction of such intercomparisons: Vector Comparison Matrix (VCM) plots. A VCM is an $N \times N$ matrix whose lower left triangle elements M_{ij} show the normalized dot product (i.e., the pattern correlation r_{ij}) of the i -th and j -th vectors in the intercomparison set of N vectors, and whose upper right triangle elements M_{ij} show the r.m.s. magnitude ratio ($M_{ij} = A_j/A_i$) of those vectors. By definition, all diagonal elements M_{ii} are equal to 1.

The pattern correlations and magnitude ratios of all possible pairs in the set of 163 simulated trend fields are shown in Fig. 2b for air temperature and precipitation. The VCMs generally reveal a greater pattern consistency of the trends in the prescribed-SST simulations (GLB as well as TRP) than in the coupled simulations, especially for precipitation. This in itself is not surprising. After all, the GLB and TRP simulations use the observed history of SSTs over 1951-1999, whereas the SSTs are different in each of the 76 coupled simulations. Nonetheless, this greater consistency suggests a significant constraining influence of the SSTs on the climate trends over land. Furthermore, the fact that the GLB and TRP simulations are just as mutually consistent as they are internally consistent suggests that the tropical SSTs are especially important in providing this constraining influence.

The tropical influence becomes even more obvious upon comparing the ensemble-mean trend fields in the three separate simulation groups (CPL, GLB, and TRP) with one another and with the observed trend field. This is done in Fig. 2c, in the same VCM format. Again, consistent with a strong influence of SSTs on the trends over land, the pattern correlations with observations of the ensemble-mean trends in the prescribed-SST simulations (exceeding 0.7 for air temperature as well as precipitation) are higher than of those in the coupled simulations (0.3 and 0.4 for air temperature and precipitation, respectively). And again, consistent with the SST influence being associated primarily with the tropical SSTs, the ensemble-mean trend patterns in the tropically and globally prescribed SST simulations are correlated at levels exceeding 0.9 for both air temperature and precipitation.

Given the chaotic nature of the climate system, one may regard each of our 163 simulated trend fields as comprising a forced climate signal plus unpredictable climate noise. One would therefore not expect any of the individual simulated trend fields to agree perfectly with the observed trend fields, or with one another, even if the models were "perfect". Even in such a scenario, however, the large discrepancies of the simulations with respect to both observations and one another in Figs. 2a and 2b would suggest a substantial unpredictable noise component in trends over intervals as long as 50 years, with important implications for adaptation and mitigation strategies in response to climate projections over such intervals. This noise component is greatly reduced, though not completely eliminated, by ensemble-averaging the trends in our CPL, GLB, and TRP simulations, which leads to a better estimate of the forced signal in each of these

simulation groups. However, the observed trend retains its noisy part, and so the agreement between the ensemble-averaged model trends and observed trends remains imperfect in Fig. 2c, and would remain imperfect even if the models were perfect.

Figure 2 also provides an assessment of the accuracy and consistency of the magnitudes of the spatially varying parts of the simulated trend fields. Compared to observations, the magnitudes of both the precipitation and surface temperature trends are generally smaller in the coupled simulations than in the prescribed-SST simulations. Reducing the noise through ensemble averaging, as done in Fig. 2c, brings out these aspects of the simulations more clearly, and shows that the magnitudes in the prescribed-SST simulations are also more realistic. The fact that the magnitudes in the prescribed tropical-SST simulations are close to those in the prescribed global-SST simulations again highlights the critical influence of the tropical SSTs on these remote trends.

4 Observed and simulated tropical SST trends

In reality, of course, model errors also contribute to the disagreements with observations evident in Figs. 1 and 2. Ascertaining their sources and importance relative to climate noise presents an interesting challenge. The strong influence of the tropical SSTs suggests that we take a closer look at the tropics. Figure 3 compares the ensemble-mean tropical SST trend map from the coupled simulations with the observed trend map. The latter is derived from an unweighted average of observations compiled at the UK Met Office's Hadley Centre (Rayner et al. 2003), the Lamont-Doherty Earth Observatory (Kaplan et al. 1998), and NOAA (Smith and Reynolds 2005). The dominant impression

from this figure is that although the coupled simulations are realistic in capturing the observed overall tropical warming trend, they underestimate the substantial spatial variation of that observed warming trend.

Figure 4 provides a quantitative comparison of the tropical SST trend field in each of the 76 coupled simulations with the observed trend field, separately for just the area-mean trends (Fig. 4a), the full trend fields (Fig. 4b), and just the spatially varying parts of the trend fields (Fig. 4c). Consistent with the impression from Fig. 3, the pattern correlations of the observed and ensemble-mean simulated trend fields are quite high (~ 0.8) if the area means are retained, but drop to ~ 0.3 when the area means are removed. Not surprisingly, the individual model fields are correlated with the observed field at even lower levels than is the ensemble-mean field, although some do show higher correlations. The magnitude of the spatially varying part is also generally underestimated. Interestingly, although the area-mean trends in the individual simulations show a large spread around the observed area-mean trend (Fig. 4a), the multi-model ensemble-mean area-mean trend is nearly perfect in this regard.

It is remarkable that the majority of the 76 simulated tropical SST trend fields have pattern correlations with the observed trend field of lower than 0.3 after their area means are removed. Such a poor correspondence can arise either from the tropical SST evolution being so chaotic even on multi-decadal scales as to overwhelm the spatially varying part of the radiatively forced warming signal, or from model error. To clarify the issue, we performed extensive Monte Carlo significance tests. Specifically, we generated

10000 Monte Carlo samples of 76 vectors drawn from a multi-normal probability distribution with the same mean and covariance statistics as our 76 simulated tropical SST trend vectors, and identified the vector in each sample having the maximum pattern correlation with the observed trend vector. A histogram of the 10000 such maximum correlations was constructed. The mean of this distribution was 0.57, consistent with the maximum correlation of 0.57 in Fig. 4c, and with not a single value out of the 10000 exceeding 0.76. To appreciate the significance of these numbers, we generated an additional sample of 76 vectors, compared the vectors in the 10000 samples with all the vectors in this 10001st sample in turn, and constructed a similar histogram of maximum pattern correlations. This distribution had a mean of 0.85 and a standard deviation of 0.025. In other words, for the spatially varying part of the observed trend vector to be consistent with the distribution of the 76 coupled model simulated trend vectors, one would expect the maximum correlation in Fig. 4c with the observed vector to lie between 0.77 and 0.93 with 99.9% probability (as indicated by the gray shaded region on Fig. 4c), in sharp contrast to the value of 0.57 actually obtained. This provides strong evidence that *the spatial pattern of the observed tropical SST trend field lies well outside the space of the spatially varying patterns of the simulated trend fields*, and points to model error as a major contributor to the poor correspondence of the observed and simulated trends in Fig. 4c, and also in Fig. 4b.

5 Impact of SST biases in the coupled simulations

Thus far, our analysis has shown that the recent half-century trends in the Atlantic Rim regions were strongly affected by the tropical SST trends, and that the IPCC/AR4

coupled models were deficient in capturing the spatial variation of both sets of trends. One is tempted to conclude that these deficiencies are directly related. Before doing so, however, one needs to consider another possibility, that the errors in the Atlantic Rim trends are not entirely due to errors in the tropical SST trends *per se*, but also partly due to errors in the generation mechanisms of remote responses to tropical SST changes, associated with various climate biases in the coupled models. For concreteness, let us consider a simplified linear framework in which the remote anomaly response vector \mathbf{y} to a tropical SST anomaly forcing vector \mathbf{x} is expressed as $\mathbf{y} = \mathbf{G}(\mathbf{X}) \mathbf{x}$, in which the "Green's Function" response matrix \mathbf{G} depends upon the mean tropical SST climatology \mathbf{X} . It is then clear that that an error in \mathbf{y} can arise from errors in both \mathbf{x} and \mathbf{X} . So, although we have shown that the coupled models have errors in their tropical SST trend vectors \mathbf{x} , it remains to be assessed to what extent those errors, and not biases in \mathbf{X} , are the main contributors to the errors in the Atlantic Rim trends \mathbf{y} .

The substantial biases of the IPCC AR4 coupled models in the tropics have been documented elsewhere (e.g., Lin 2007). In a study such as ours, one way to address the impact of the tropical SST biases on the Atlantic Rim trends could be through TRP-type uncoupled atmospheric GCM simulations using one specific GCM, in which the time-varying tropical SST anomaly fields for 1951-1999 from the 76 coupled simulations (determined with respect to the models' 1951-1999 SST climatology) are prescribed on top of the *observed* 1951-1999 SST climatology, generating an ensemble of simulations for each SST forcing series. One could then compare the ensemble-mean remote response trend \mathbf{y} obtained for each anomalous SST forcing series with that obtained for the

observed anomalous SST forcing series. The difference would be entirely due to errors in the simulated SST anomalies, since the error in the SST climatology would be zero by prescription. Performing such a computationally expensive numerical experiment is beyond the scope of this study. Fortunately, the issue can be addressed much more cheaply under the linear approximation $\mathbf{y} = \mathbf{G}(\mathbf{X}) \mathbf{x}$, whose validity has been demonstrated in several studies (e.g, Barsugli and Sardeshmukh 2002, Schneider et al 2003, Barsugli et al 2006). Under this approximation, one could estimate the Green's Function operator $\mathbf{G}(\mathbf{X})$ for one specific atmospheric GCM, and directly estimate the impact of errors in the coupled-model simulated tropical SST trends \mathbf{x} on the Atlantic Rim trends \mathbf{y} using the above linear equation.

The specific atmospheric GCM we chose for this diagnosis was the Max Plank Institute of Meteorology's atmospheric GCM ECHAM5 (Roeckner et al. 2006), which utilizes a spatial discretization of T42 in the horizontal ($\sim 2.8^\circ$ in latitude and longitude) and 19 levels in vertical. We estimated $\mathbf{G}(\mathbf{X})$ by determining the GCM's global atmospheric responses to localized SST anomaly "patches" imposed on top of the observed SST climatological annual cycle at 43 regularly spaced locations throughout the tropical oceans. The experimental set-up and methodology were identical to that in our previous study using the National Center for Atmospheric Research atmospheric GCM CCM3 (Barsugli et al. 2006). The locations and patterns of SST patches are shown in Fig. 5. Specifying an area-average SST anomaly magnitude of about 0.66°C over each patch, 20-member ensemble integrations were performed for both warm and cold patch forcing

for 25 months starting 1 October. The global linear response to each patch forcing was defined as one-half of the difference between the responses to warm and cold forcing, and identified with a column of the Green's Function matrix $\mathbf{G}(\mathbf{X})$.

Determining such a $\mathbf{G}(\mathbf{X})$ gives one the ability to estimate the global response to an arbitrary tropical SST anomaly field \mathbf{x} as $\mathbf{y} = \mathbf{G}(\mathbf{X}) \mathbf{x}$, i.e. as a weighted sum of the responses to the individual patches, with weights that are proportional to the amplitude of \mathbf{x} over the patches. The details of this procedure are given in Barsugli et al. (2006) and are not repeated here. In effect, such a linear reconstruction amounts to an extremely inexpensive estimation of the global linear response to tropical SST changes. The linearly reconstructed responses of surface air temperature and precipitation over our Atlantic Rim land masses to the observed tropical SST trend forcing are shown in Fig. 6b. They compare very well with the corresponding ensemble-mean trends shown in Fig. 6a obtained from the fully nonlinear 16-member ensemble ECHAM5 GLB simulations of 1951-1999 (Table 4), in terms of both pattern correlation and r.m.s magnitude, thus providing a strong justification of our linear diagnostic approach¹.

Figure 6c shows the pattern correlations and r.m.s. magnitude ratios of the linearly reconstructed trend responses over the Atlantic Rim land masses to the coupled-model

¹ We also reconstructed the trends using a $\mathbf{G}(\mathbf{X})$ derived from the CCM3 patch experiment (Barsugli et al. 2006), and compared them over the Atlantic Rim land masses with the ensemble-mean trends from the CCM3 GLB simulations (Table 2). The pattern correlations (r.m.s. magnitude ratios) were 0.70 (0.85) and 0.92 (1.11) for surface temperature and precipitation. With the land-averaged trends removed, the pattern correlations (r.m.s. magnitude ratios) were 0.68 (0.88) and 0.92 (1.10) for surface and temperature and precipitation.

simulated tropical SST trends with the corresponding observed trend fields. As in Fig. 2, only the spatially varying parts of the trend fields are compared. Interestingly, reducing (although not completely eliminating) the effect of the tropical SST biases by using the same “correct” $\mathbf{G}(\mathbf{X})$ operator in all cases yields a much improved simulation of the remote air temperature trend. Indeed the skill of the reconstructed air temperature trend using the simulated ensemble-mean SST trend field is now close to that obtained using the observed SST trend field, which is itself very close to skill of the ensemble-mean air temperature trend in the ECHAM5 GLB simulations². The improvement is not as marked in the simulation of the remote precipitation trends. Overall, this linear diagnosis suggests that the tropical SST biases (i.e. the errors in \mathbf{X}) of the coupled models have a much greater impact on the simulation of the remote temperature trends than the remote precipitation trends. Note however, that the errors in \mathbf{x} do matter even for the remote temperature trends, as confirmed through additional numerical experiments described below.

6 Impact of spatial variations of the tropical SST trend

Given the importance of the tropical SST trend \mathbf{x} in generating the remote trends \mathbf{y} in our Atlantic Rim regions, we provide further evidence that the spatially varying part of \mathbf{x} is important in this regard. For convenience let us write \mathbf{x} as a sum of its tropically averaged and spatially varying parts as $\mathbf{x} = [\mathbf{x}] + \mathbf{x}^*$. The main conclusion from Fig. 4 was that the multi-model ensemble-mean $[\mathbf{x}]$ from our set of 76 coupled simulations matches

² Note that although the observed tropical SST trends are identical in the reconstruction and the GLB simulations, they produce slightly different trend responses around the globe because the reconstruction is linear and the GLB simulations are nonlinear.

the observed $[\mathbf{x}]$ ($= 0.43$ °C per 50 years) almost perfectly, but the spatially varying part \mathbf{x}^* does not. To assess the impact of $[\mathbf{x}]$ on \mathbf{y} , we performed three additional 50-year integrations with the ECHAM5 model (see Table 4): a control run (CTL) with climatological SSTs \mathbf{X} , another run (TRF) with $\mathbf{X} + \mathbf{x}$, and a third run (TRM) with $\mathbf{X} + [\mathbf{x}]$. The Atlantic Rim responses of surface air temperature and precipitation to the \mathbf{x} and $[\mathbf{x}]$ trend forcings are shown in Figs. 7a and 7b, respectively. The responses to the \mathbf{x} trend forcing are very similar to the trends obtained in the ECHAM GLB simulations (Fig. 6a), with pattern correlations exceeding 0.8. The responses to the $[\mathbf{x}]$ trend forcing, however, differ substantially from the trends in the ECHAM GLB simulations, especially for precipitation (see also Table 5). The remote temperature response is relatively less affected by ignoring \mathbf{x}^* , but the pattern correlation of its spatially varying part with that of the ECHAM5 GLB temperature trend field is still modest (0.51).

The distinction between the dynamics of the remote air temperature and precipitation trend responses arises basically from the fact that air temperature is related to geopotential heights whereas precipitation is related to jet structure i.e. to the horizontal gradients of the geopotential heights. The relatively stronger impact of \mathbf{x}^* on the remote precipitation trend is thus associated with a relatively stronger impact of \mathbf{x}^* on the strength and position of the upper tropospheric jets. Figure 8 shows the ensemble-mean 50-year trends of northern hemispheric 200 hPa heights and zonal winds and tropical precipitation in the GLB simulations, alongside the corresponding responses to the \mathbf{x} and $[\mathbf{x}]$ tropical SST trend forcings in the TRF and TRM experiments. As in Fig 7, the responses to the \mathbf{x} forcing clearly compare much better with the GLB trends than do the

responses to the $[\mathbf{x}]$ forcing. In particular, including the \mathbf{x}^* portion in the \mathbf{x} trend forcing yields a much stronger tropical precipitation response and a much stronger 200 hPa jet response, especially over the PNA sector. The spatially uniform $[\mathbf{x}]$ forcing produces a much weaker tropical precipitation response and consequently a much weaker 200 hPa jet response. The unrealistically weak amplitude of \mathbf{x}^* in the coupled simulations (Fig. 4) is thus the primary cause of the unrealistically weak amplitude and poor geographical structure of the remote precipitation trends over the Atlantic Rim land masses in those simulations.

7 Observed and simulated drought trends

Given the considerable uncertainty and/or error in capturing the recent trends of surface air temperature and precipitation on regional scales in the coupled simulations, one might wonder how similar uncertainties and/or errors in regional climate projections might impact mitigation and adaptation responses to climate change. One way to address this issue, especially from a socio-economically relevant drought perspective (Wilhite 2000), is to examine trends in a drought index such as the PDSI. The PDSI is a combined integral measure of anomalous surface air temperature and precipitation for assessing the deficiency or surplus of soil moisture. As a widely used hydroclimatic indicator, it has proven to be an effective measure of long-term droughts and wet spells (Dai et al. 1998; Dai et al. 2004).

We estimated the 1951 to 1999 trends of annual-mean PDSI over the non-glaciated portions of our Atlantic Rim land masses of interest using observations as well as all our

163 model simulations. The monthly PDSI values P_j in the simulations were estimated from a PDSI model (Palmer 1965) at each grid point as,

$$P_j = 0.897 P_{j-1} + \frac{1}{3} K d_j,$$

where K is Palmer's "climate characteristic" at the grid point, and d_j is the difference between the actual precipitation in month j and the expected precipitation needed to maintain a normal soil moisture level, which is a function of surface air temperature and precipitation. We calibrated this model using unweighted averages of surface air temperature and precipitation records in the period 1979-1999, in which the quality and quantity of observations were greatly improved due to the availability of satellite data. The specification of water holding capacity in the PDSI model was based on the climatology compiled by Webb et al. (1993).

The observed PDSI trend map is shown in Fig. 9a, and similar trend maps derived from the ensemble means of the 76 CPL, 66 GLB, and 21 TRP simulations are shown in Figs. 9b and 9c. The coupled simulations indicate a trend pattern of widespread drought that is seriously at odds with the observations. The fact that over most of North America even the sign of the simulated trend is opposite to that of the observed is disturbing. The uncoupled simulations with prescribed observed SSTs are generally more realistic in this regard, although not over Northern Europe. And again, the simulations with prescribed tropical SST changes are just as realistic as those with prescribed global SST changes. The poor representation of tropical SST trends in the coupled simulations is thus also

implicated in the poor representation of these socio-economically important PDSI trends³.

8 Summary and discussion

We find that the patterns of recent climate trends over North America, Greenland, Europe, and North Africa are generally less well captured by state-of-the-art coupled atmosphere-ocean models with prescribed observed radiative forcing changes than even by uncoupled atmospheric models without those radiative forcing changes, but with the observed SST changes prescribed only in the tropics. The basic reason for this is that tropical SSTs are poorly represented in the coupled simulations. Errors in representing both the observed SST climatology and the spatial variation of the SST trends are important. The latter error, in particular, has a large impact on the simulation of both local and remote precipitation trends. The sensitivity of the global mean climate to the pattern of tropical oceanic warming has already been highlighted in some recent studies (e.g., Barsugli et al. 2006). Our study provides evidence of a similar large sensitivity also of regional climate changes, even in regions remote from the tropics. The fact that even with full atmosphere-ocean coupling, climate models with prescribed observed radiative forcing changes do not capture the pattern of the observed tropical oceanic warming suggests that either the radiatively forced component of this warming pattern was sufficiently small in recent decades to be dwarfed by natural tropical SST variability, or that the coupled models are misrepresenting some important tropical physics. We have

³ Dai et al. (2004) show that the global PDSI trends over 1950-2002 can be mostly explained by changes of precipitation (see their Fig. 7). The poor representation of the PDSI trends in the coupled simulations in Fig. 9 is also mostly associated with the poor representation of the regional precipitation trends in those simulations, which is itself strongly associated with the poor representation of the spatial variation of the tropical SST trends in those simulations.

argued that the discrepancy of the simulated trends with respect to observations is not entirely due to climate noise but is at least partly due to model errors. The existence of tropical SST biases in the coupled models, whose impact on remote trends is also significant, further supports our argument. If correct, our assessment would raise the hope that reducing such tropical SST errors would lead to significantly improved regional climate predictions around the globe.

Acknowledgments We thank E. Schneider for his comments on an earlier version of manuscript that helped clarify the role of the tropical SST biases on remote trends in the coupled model simulations. The Max Planck Institute for Meteorology kindly provided the ECHAM5 code used in this study. Our own simulations were performed at the NOAA ESRL High Performance Computing Systems (HPCS) facility. This work was partly supported by NOAA's Climate Program Office.

References

- Anderson JL et al (2004) The new GFDL global atmosphere and land model AM2-LM2: evaluation with prescribed SST simulations. *J Clim* 17:4641-4673
- Barnston AG, Kumar A, Goddard L, Hoerling MP (2005) Improving seasonal prediction practices through attribution of climate variability. *Bull Amer Meteor Soc* 86:59-72
- Barsugli JJ, Sardeshmukh PD (2002) Global atmospheric sensitivity to tropical SST anomalies throughout Indo-Pacific basin. *J Clim* 15:2205-2231
- Barsugli JJ, Shin S-I, Sardeshmukh PD (2006) Sensitivity of global warming to the pattern of tropical ocean warming. *Clim Dyn* 27:483-492
- Bracco A, Kucharski F, Kallummal R, Molteni F (2004) Internal variability, external forcing and climate trends in multi-decadal AGCM ensembles. *Clim Dyn* 23:659-678
- Chen M, Xie P, Janowiak JE, Arkin PA (2002) Global land precipitation: A 50-yr monthly analysis based on gauge observations. *J of Hydrometeorology* 3:249-266
- Collins WD et al (2006) The community climate system model version 3 (CCSM3). *J Clim* 19:2122–2143
- Compo GP, Sardeshmukh PD (2009) Oceanic influences on recent continental warming. *Clim Dyn* 32:333-342
- Dai AG, Trenberth KE, Karl TR (1998) Global variations in droughts and wet spells: 1900-1995. *Geophys Res Lett* 25:3367-3370

- Dai AG, Trenberth KE, Qian T (2004) A global dataset of Palmer Drought Severity Index for 1870-2002: Relationship with soil moisture and effects of surface warming. *J of Hydrometeorology* 5:1117-1130
- Delworth TL et al (2006) GFDL's CM2 global coupled climate models. Part I: Formulation and simulation characteristics. *J Clim* 19:643–674
- Deser C, Phillips AS, Hurrell JW (2004) Pacific interdecadal climate variability: Linkages between the tropics and the North Pacific during boreal winter since 1900. *J Clim* 17:3109-3124
- Deser C, Phillips AS (2009) Atmospheric circulation trends, 1950-2000: The relative roles of sea surface temperature forcing and direct atmospheric radiative forcing. *J Clim* 22:396-413
- Furevik T, Bentsen M, Drange H, Kindem IKT, Kvamtsø NG, Sorteberg A (2003) Description and evaluation of the Bergen climate model: ARPEGE coupled with MICOM. *Clim Dyn* 21:27–51
- Folland CK, Sexton DMH, Karoly D, Johnson C, Rowell D, Parker D (1998) Influences of anthropogenic and oceanic forcing on recent climate change. *Geophys Res Lett* 25:353-356
- Gates WL (1992) AMIP: The atmospheric model intercomparison project. *Bull Amer Meteor Soc* 73:1962-1970
- Goddard L, Mason SJ, Zebiak SE, Ropelewski CF, Basher R, Cane MA (2001) Current approaches to seasonal to interannual climate predictions. *Int J Climatol* 21:1111-1152

- Gordon C et al (2000) The simulation of SST, sea ice extents and ocean heat transport in a version of the Hadley Centre coupled model without flux adjustments. *Clim Dyn* 16:147–168
- Gordon HB et al (2002) The CSIRO Mk3 climate system model. Tech. Rep. 60, CSIRO Atmospheric Research, Aspendale, Victoria, Australia, pp 134
- Graham NE (1994) Decadal-scale climate variability in the tropical and North Pacific during the 1970s and 1980s: Observations and model results. *Clim Dyn* 10:135–162
- Gualdi S, Scoccimarro E, Navarra A (2006) Changes in tropical cyclone activity due to global warming: Results from a high-resolution coupled general circulation model. *J Clim* 21: 5204–5228
- Hansen JE et al. (2001) A closer look at United States and global surface temperature change. *J Geophys Res* 106:23947-23963
- Hansen JE et al. (2007) Climate simulations for 1880–2003 with GISS modelE. *Clim Dyn* 29:661-696
- K-1 model developers (2004) K-1 coupled model (MIROC) description. K-1 Tech. Rep. 1 [Hasumi H, Emori S (eds.)], Center for Climate System Research, University of Tokyo, pp 34
- Herweijer C, Seager R (2008) The global footprint of persistent extra-tropical drought in the instrumental era. *Int J Climatol* DOI:10.1002/joc.1950
- Hoerling MP, Hurrell JW, Xu T (2001) Tropical origins for recent North Atlantic climate change. *Science* 292:90-92
- Hoerling MP, Kumar A (2003) The perfect ocean for drought. *Science* 299:691-699

- Hurrell JW, Hoerling MP, Phillips AS, Xu T (2004) Twentieth century North Atlantic climate change. Part I: assessing determinism. *Clim Dyn* 23:371-389
- Hurrell JW, Hack JJ, Phillips AS, Caron J, Yin J (2006) The dynamical simulation of the community atmosphere model version 3 (CAM3). *J Clim* 19:2162-2183
- IPCC (2007) *Climate Change 2007: The Physical Science Basis. Contribution of Working Group I to the Fourth Assessment Report of the Intergovernmental Panel on Climate Change* [Solomon S, Qin D, Manning M, Chen Z, Marquis M, Averyt K, Tignor MMB, Miller HL (eds.)]. Cambridge University Press, Cambridge, United Kingdom and New York, pp 996
- Johns T et al (2006) The new Hadley Centre climate model HadGEM1: Evaluation of coupled simulations. *J Clim* 19:1327-1353
- Jungclaus J et al (2006) Ocean circulation and tropical variability in the coupled model ECHAM5/MPI-OM. *J Clim* 19:3952–3972
- Kaplan A, Cane M, Kushnir Y, Clement A, Blumenthal M, Rajagopalan B (1998) Analyses of global sea surface temperature 1856-1991. *J Geophys Res* 103:18567-18589
- Kim SJ, Flato GM, de Boer GJ, McFarlane NA (2002) A coupled climate model simulation of the Last Glacial Maximum. Part I: Transient multi-decadal response. *Clim Dyn* 19:515–537
- Lau N-C, Nath MJ (1994) A modeling study of the relative roles of tropical and extratropical SST anomalies in the variability of the global atmosphere-ocean system. *J Clim* 7:1184-1207

- Lau N-C (1997) Interactions between global SST anomalies and the midlatitude atmospheric circulation. *Bull Amer Meteor Soc* 78:21-33
- Lin JL (2007) The double-ITCZ problem in IPCC AR4 coupled GCMs: Ocean-atmosphere feedback analysis. *J Clim* 20:4497-4525
- Lucarini L, Russell GL (2002) Comparison of mean climate trends in the northern hemisphere between National Centers for Environmental Prediction and two atmosphere-ocean model forced runs. *J Geophys Res* 107:4269. doi:10.1029/2001JD001247
- Marti O et al (2005) The new IPSL climate system model: IPSL-CM4. Tech. Rep., Institut Pierre Simon Laplace des Sciences de l'Environnement Global, IPSL, Case 101, Paris, France, pp 86
- Min S-K, Legutke S, Hense A, Kwon W-T (2005) Internal variability in a 1000-yr control simulation with the coupled model ECHO-G-I: Near-surface temperature, precipitation and mean sea level pressure. *Tellus* 57A:605–621
- Mitchell TD, Jones PD (2005) An improved method of constructing a database of monthly climate observations and associated high-resolution grids. *Int J Climatol* 25:693-712
- Palmer WC (1965) Meteorological drought. Research Paper 45, U.S. Dept. of Commerce, pp. 58
- Ray AJ et al. (2008) Climate Change in Colorado: A Synthesis to Support Water Resources Management and Adaptation. A Report for the Colorado Water Conservation Board, University of Colorado at Boulder, pp 52

- Rayner NA, Parker DE, Horton EB, Folland CK, Alexander LV, Rowell DP, Kent EC, Kaplan A (2003) Global analyses of sea surface temperature, sea ice, and night marine air temperature since the late nineteenth century. *J Geophys Res* 108:4407-4443 (doi:10.1029/2002JD002670)
- Roeckner E et al (1996) The atmospheric general circulation model ECHAM4: Model description and simulation of present-day climate. Max Planck Institute for Meteorology Rep 218, Hamburg, Germany, pp 90
- Roeckner E et al (2006) Sensitivity of simulated climate to horizontal and vertical resolution in the ECHAM5 atmosphere model. *J Clim* 19:3771-3791
- Rodwell MJ, Rowell DP, Folland CK (1999) Oceanic forcing of the wintertime North Atlantic Oscillation and European climate. *Nature* 398:320-323
- Rudolf B, Beck C, Grieser J, Schneider U (2005) Global precipitation analysis products. Global Precipitation Climatology Centre (GPCC), DWD, Internet Publication, 1-8
- Salas-Mélia D et al (2005) Description and validation of the CNRM-CM3 global coupled model, CNRM working note 103.
- Saravanan R (1998) Atmospheric low-frequency variability and its relationship to mid latitude SST variability: studies using the NCAR climate system model. *J Clim* 11:1386-1404
- Sardeshmukh PD, Hoskins BI (1984) Spatial Smoothing on the Sphere. *Mon Wea Rev* 112:2524-2529.
- Schneider EK, Bengtsson L, Hu Z (2003) Forcing of northern hemisphere climate trends. *J Atmos Sci* 60:1504-1521

- Schubert SD, Suarez MJ, Region PJ, Koster RD, Bacmeister JT (2004) On the cause of the 1930s Dust Bowl. *Science* 303:1855-1859
- Sidall M, Kaplan MR (2008) Climate science: A tale of two ice sheets. *Nature Geosci* 1:570-572
- Smith TM, Reynolds RW (2005) A global merged land-air-sea surface temperature reconstruction based on historical observations (1880-1997). *J Clim* 18:2021-2036
- Sutton RT, Hodson DLR (2003) The influence of the ocean on North Atlantic climate variability 1871-1999. *J Clim* 16:3296-3313
- Taylor KE (2001) Summarizing multiple aspects of model performance in a single diagram. *J Geophys Res* 106:7193-7192
- Volodin EM, Diansky NA (2004) El Niño reproduction in coupled general circulation model. *Russ Meteor Hydrol* 12:5–14
- Washington WM et al (2000) Parallel climate model (PCM) control and transient simulations. *Clim Dyn* 16:755–774
- Webb RS, Rosenzweig CE, Levine ER (1993) Specifying land surface characteristics in general circulation models: Soil profile data set and derived water holding capacities. *Global Biogeochem Cycles* 7:97-108
- Wilhite DA (2000) Drought as a natural hazard: Concepts and definitions. *Drought: A Global Assessment*, Wilhite DA, Ed., Routledge, 3-18
- Yu Y, Zhang X, Guo Y (2004) Global coupled ocean- atmosphere general circulation models in LASG/IAP. *Adv Atmos Sci* 21:444-455

Yukimoto S, Noda A (2002) Improvements in the Meteorological Research Institute global ocean-atmosphere coupled GCM (MRI-CGCM2) and its climate sensitivity. Tech. Rep. 10, NIES, Japan, pp 8

Figure Legends

Fig. 1 Trends of annual-mean surface air temperature (*left*) and precipitation (*right*) over 1951-1999 derived from (a) observations, (b) multi-model ensemble-mean coupled climate model simulations, and (c) multi-model ensemble-mean uncoupled atmospheric model simulations with prescribed observed time varying SSTs. Annual averages are over July to June. All simulation and observational data were interpolated to a common $\sim 2.8^\circ \times 2.8^\circ$ latitude-longitude grid and then truncated to total spherical wavenumber 12 to emphasize subcontinental-scale features (Sardeshmukh and Hoskins 1984).

Fig. 2 (a) Taylor diagram comparisons of simulated and observed trends over 1951-1999 of surface air temperature (*left*) and precipitation (*right*) over land areas in the region 20° to 75°N , 170°W to 40°E . Each dot depicts the pattern correlation r (along the angular coordinate) and r.m.s. magnitude ratio A (along the radial coordinate) of a simulated trend field and the observed trend field. Red dots: coupled simulations (CPL); Dark blue squares: uncoupled simulations with prescribed global SST changes (GLB); Orange squares: uncoupled GLB simulations with additional prescribed radiative forcing changes; Light blue squares: uncoupled simulations with SST changes prescribed only in the tropics (TRP). For reference, the temperature and precipitation trend fields obtained from the individual observational datasets (black triangles) are also compared with the average of these observational datasets. (b) Vector Comparison Matrices (VCMs) of the trend vectors from the 76 CPL, 66 GLB, and 21 TRP simulations. The lower left triangle depicts the pattern correlations r_{ij} and the upper right elements depict the r.m.s. magnitude

ratio A_j/A_i of each pair i,j among the 163 simulated trend vectors. (c) VCMs of the simulated ensemble-mean and observed trend vectors.

Fig. 3 Trends of annual-mean tropical (30°S-30°N) SSTs over 1951-1999 derived from (a) observations and (b) the multi-model ensemble-mean of the coupled simulations. All simulation and observational data were interpolated to a common $\sim 2.8^\circ \times 2.8^\circ$ latitude-longitude grid and then truncated to total spherical wave number 21 to focus on the comparisons of larger scale features (Sardeshmukh and Hoskins 1984).

Fig. 4 (a) Estimated probability density function of the magnitude ratio of the 76 area-averaged simulated tropical SST trends with the observed trend. (b) Taylor diagram comparisons of the simulated and observed tropical SST trend fields with their areal means retained. (c) Taylor diagram comparisons of the simulated and observed tropical SST trend fields with their areal means removed. Red dots: coupled simulations (CPL); Black squares: ensemble-mean of coupled simulations. For reference, the trend fields obtained from the individual observational datasets (black triangles) are also compared with the average of these observational datasets. The gray shading in (b, c) indicates 99.9% probability bounds for the observed trend vector to be consistent with the probability distribution of the 76 simulated trend vectors (see text for details).

Fig. 5 The location of the SST anomaly patches prescribed in the SST patch experiments. For reference, the standard deviation of annually averaged tropical SSTs from the HadISST dataset (Rayner et al. 2003) during 1951-1999 is also shown. Note that the

Indo-Pacific and Atlantic patches are of different sizes. Their full extent is illustrated by the gray-shaded patches at the bottom of figure for the Indo-Pacific (*left*) and Atlantic (*right*) patches.

Fig. 6 (a) Trends of annual-mean surface air temperature (*left*) and precipitation (*right*) over 1951-1999 derived from the ensemble-mean uncoupled ECHAM5 simulations with prescribed global SST changes (ECHAM5 GLB; see Table 4). (b) The linearly reconstructed trend response to the observed tropical SST trend over 1951-1999 using a linear response operator G estimated from independent patch experiments. The pattern correlation r and r.m.s. magnitude ratio A of the fields in (a) and (b) with their area means retained, and r^* and A^* with their area means removed, are also shown. (c) Pattern correlation and r.m.s. magnitude ratio with respect to observations of the linearly reconstructed surface air temperature (*left*) and precipitation (*right*) trends over the land areas in (a) and (b). The filled black and red circles show the results for the ensemble-mean trends obtained in the uncoupled ECHAM5 GLB and coupled IPCC/AR4 simulations, and the filled black and red squares show the results for the linearly reconstructed trends obtained using the observed and coupled-model simulated ensemble-mean tropical SST trends. The green arrows indicate the improvement of the trend comparison with observations obtained by removing the effect of the climate biases in the coupled simulations. See text for details. All simulation and observational fields were truncated to total spherical wave number 12 to focus on the comparisons of larger scale features (Sardeshmukh and Hoskins 1984).

Fig. 7 Annual-mean response of (left) surface air temperature and (right) precipitation (a) to the observed tropical SST trend (TRF; see Fig. 3a), and (b) to its spatially uniform component (TRM). All simulation data were truncated to total spherical wave number 12 to focus on the comparisons of larger scale features (Sardeshmukh and Hoskins 1984).

Fig. 8 (a) Trends of annual-mean 200-hPa heights and zonal winds (*top*) and tropical precipitation (*bottom*) over 1951-1999 in the ensemble-mean uncoupled ECHAM5 simulations with prescribed global time-varying SSTs (ECHAM5 GLB). (b-c) Annual-mean response of 200-hPa heights and zonal winds (*top*) and tropical precipitation (*bottom*) to the (b) observed tropical SST trend (TRF, Fig. 3a), and (c) to its spatially uniform component (TRM). The zero contour in the 200-hPa height trend and response fields is thickened and negative contours are dashed.

Fig. 9 Trends of annual-mean PDSI in non-glaciated regions over 1951-1999, derived from (a) observations, (b) multi-model ensemble mean of the coupled simulations, and (c) multi-model ensemble mean of the prescribed SST simulations, with the SST changes prescribed globally (GLB) and only in the tropics (TRP). Warm and cold colors (negative and positive values) indicate a trend towards stronger and weaker droughts, respectively, over this period.

Table 1 Description of the coupled climate model simulations used. The nomenclature followed is that in the archive at the Program for Climate Model Diagnosis and Intercomparison (PCMDI). All simulations were performed as a part of IPCC's 20th century simulations using the best available estimates of the time-varying 20th century radiative forcings associated with changes in greenhouse gases, aerosols, and solar forcing. Columns show the name of the coupled climate model, the number N of ensemble members, the atmospheric horizontal discretization (s: spectral, g: gridpoint) and resolution (longitude \times latitude, number of vertical levels), the oceanic vertical coordinate (z: z-, σ : sigma-, ρ : isopycnic-, and *hy*: hybrid-coordinate) and resolution (longitude \times latitude, number of vertical levels), and the reference publication for the model. For further details of the models, see <http://www-pcmdi.llnl.gov>. All data are available at the PCMDI archive.

(Continued in next page)

Model	N	Atmosphere	Ocean	Reference
BCCR-BCM2.0	1	<i>s</i> T63, L31	ρ 1.5°×0.5-1.5°, L35	Furevik et al. (2003)
CGCM3.1(T47)	5	<i>s</i> T47, L31	<i>z</i> 1.85°×1.85°, L29	Kim et al. (2002)
CGCM3.1(T63)	1	<i>s</i> T63, L31	<i>z</i> 1.4°×0.94°, L29	Kim et al. (2002)
CNRM-CM3	1	<i>s</i> T63, L45	<i>z</i> 2°×0.5-2°, L31	Salas-Mélia et al. (2005)
CSIRO-Mk3.0	3	<i>s</i> T63, L18	<i>z</i> 1.875°×0.5-0.84°, L31	Gordon et al. (2002)
CSIRO-Mk3.5	3	<i>s</i> T63, L18	<i>z</i> 1.875°×0.5-0.84°, L31	Gordon et al. (2002)
GFDL-CM2.0	3	<i>g</i> 2.5°×2°, L24	<i>z</i> 1°×1/3-1°, L50	Delworth et al. (2006)
GFDL-CM2.1	3	<i>g</i> 2.5°×2°, L24	<i>z</i> 1°×1/3-1°, L50	Delworth et al. (2006)
GISS-AOM	2	<i>g</i> 4°×3°, L12	<i>z</i> 4°×3°, L16	Lucarini and Russell (2002)
GISS-EH	5	<i>g</i> 5°×4°, L20	<i>hy</i> 2°×2°, L16	Hansen et al. (2007)
GISS-ER	9	<i>g</i> 5°×4°, L20	<i>z</i> 5°×4°, L13	Hansen et al. (2007)
FGOALS-g1.0	3	<i>s</i> T42, L26	<i>z</i> 2°×2°, L33	Yu et al. (2004)
INGV-SXG	1	<i>s</i> T106, L19	<i>z</i> 2°×1-2°, L31	Gualdi et al. (2006)
INM-CM3.0	1	<i>g</i> 5°×4°, L21	σ 2.5°×2°, L33	Volodin and Diansky (2004)
IPSL-CM4	1	<i>g</i> 3.75°×2.5°, L19	<i>z</i> 2°×1-2°, L31	Marti et al. (2005)
MIROC3.2(hires)	1	<i>s</i> T106, L53	<i>z</i> 0.28125°×0.1875°, L47	K-1 model developers (2004)
MIROC3.2(medres)	3	<i>s</i> T42, L20	<i>z</i> 1.4°×0.5-1.4°, L43	K-1 model developers (2004)
ECHO-G	5	<i>s</i> T30, L19	<i>z</i> 2.8°×0.5-2.8°, L20	Min et al. (2005)
ECHAM5/MPI-OM	4	<i>s</i> T63, L31	<i>z</i> 1.5°×1.5, L40	Jungclaus et al. (2006)
MRI-CGCM2.3.2	5	<i>s</i> T42, L30	<i>z</i> 2.5°×0.5-2.0°, L23	Yukimoto and Noda (2002)
CCSM3	8	<i>s</i> T85, L26	<i>z</i> 1.1°×0.27-1.1°, L40	Collins et al. (2006)
PCM	4	<i>s</i> T42, L18	<i>z</i> 2/3°×1/2°, L32	Washington et al. (2000)
UKMO-HadCM3	2	<i>g</i> 3.75°×2.5°, L19	<i>z</i> 1.25°×1.25, L30	Gordon et al. (2000)
UKMO-HadGEM1	2	<i>g</i> 1.875°×1.25°, L38	<i>z</i> 1.°×1/3-1°, L40	Johns et al. (2006)

Table 2 Description of the uncoupled atmospheric GCM simulations used. All simulations were performed by prescribing the observed time history of global SSTs as lower boundary conditions. Columns show the name of the model, the number N of simulations, the horizontal discretization (s: spectral, g: gridpoint) and resolution (longitude \times latitude, number of vertical levels), and the reference publication for the ensemble.

Model	N	Horizontal discretization and resolution		Reference
GFDL-AM2.14 ^{a,c}	10	<i>g</i>	2.5° \times 2°, L24	Anderson et al. (2004)
NCAR-CCM3	12	<i>s</i>	T42, L18	Hurrell et al. (2004)
ECHAM4.5 ^c	24	<i>s</i>	T42, L18	Roeckner et al. (1996)
NCAR-CAM3 ^a	5	<i>s</i>	T85, L26	Hurrell et al. (2006)
NCAR-CAM3 ^a	5	<i>s</i>	T42, L26	Hurrell et al. (2006)
NCAR-CAM3 ^{a,b}	5	<i>s</i>	T85, L26	Deser and Phillips (2008)
NCAR-CAM3 ^{a,b}	5	<i>s</i>	T42, L26	Deser and Phillips (2008)

^a The time history of sea-ice concentration were also prescribed.

^b The time histories of 20th century natural and anthropogenic forcings were also prescribed. These forcings are the same as in the 20th century CCSM3 simulations described in Table 1.

^c These model data are available at the International Research Institute (<http://iridl.ldeo.columbia.edu>).

Table 3 Description of the uncoupled atmospheric GCM simulations with prescribed tropical SSTs. All simulations were performed by prescribing the time history of observed SSTs in the tropical belt 30°S-30°N, and the observed long-term mean SST annual cycle outside the tropics. Columns show the name of the model, the number N of simulations, the horizontal discretization (s : spectral) and resolution (longitude \times latitude, number of vertical levels), and the reference publication for the ensemble.

Model	N	Horizontal discretization and resolution		Reference
NCAR-CCM3	11	s	T42, L18	Hurrell et al. (2004)
NCAR-CAM3	5	s	T85, L26	Deser and Phillips (2008)
NCAR-CAM3	5	s	T42, L26	Deser and Phillips (2008)

Table 4 Description of the uncoupled MPI-ECHAM5 simulations with prescribed observed SSTs. The ECHAM5 GLB simulations were performed by prescribing the observed time history of global SSTs. The CTL simulation was performed by prescribing only the observed SST climatology (long-term mean plus seasonal cycle). The TRF and TRM simulations were performed by imposing the observed tropical (30°S-30°N) SST trend forcing over 1951-1999 (expressed as an SST change over 50 years, see Fig. 3a), and only its spatially uniform part (0.43 °C), respectively, on top of the observed SST climatology. Columns show the name of the experiments, the number N of simulations for ECHAM GLB and the integration lengths for the CTL, TRF, and TRM simulations, the horizontal discretization (*s*: spectral) and resolution (longitude × latitude, number of vertical levels), and the reference publication for the experiment.

Experiment	N	Horizontal discretization and resolution		Reference
ECHAM5 GLB	16	<i>s</i>	T42, L19	Roeckner et al. (2006) ^a
CTL	50 yrs	<i>s</i>	T42, L19	
TRF	50 yrs	<i>s</i>	T42, L19	
TRM	50 yrs	<i>s</i>	T42, L19	

^a These model data are available at the International Research Institute (<http://iridl.ldeo.columbia.edu>).

Table 5 The pattern correlations and r.m.s. magnitude ratios of the surface air temperature (ΔT) and precipitation (ΔP) responses in the TRF and TRM tropical SST trend forcing experiments with respect to the ensemble-mean trends obtained in the ECHAM5 GLB simulations (Fig. 6a) over the Atlantic Rim land masses. The numbers show the results obtained when the land-averaged values are retained, and those in parentheses when they are removed, from the response and trend fields.

		Pattern correlation (r)	r.m.s. Amplitude ratio (A)
TRF-CTL	ΔT	0.83 (0.79)	0.78 (0.70)
	ΔP	0.85 (0.86)	0.86 (0.84)
TRM-CTL	ΔT	0.65 (0.51)	0.90 (0.61)
	ΔP	-0.28 (-0.29)	0.45 (0.41)

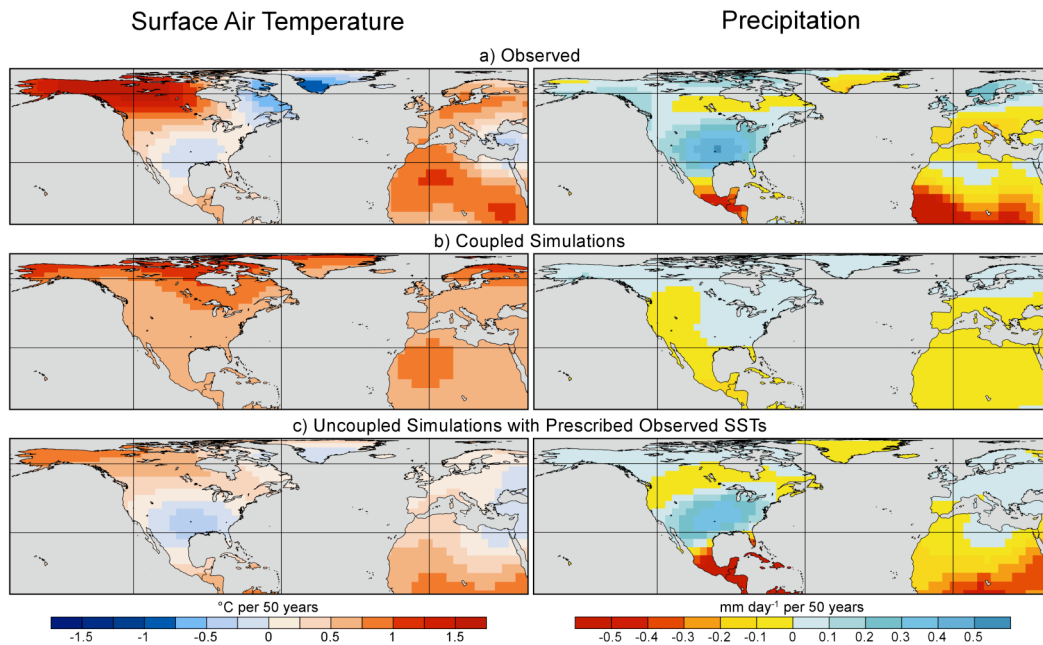


Fig. 1 Trends of annual-mean surface air temperature (*left*) and precipitation (*right*) over 1951-1999 derived from (a) observations, (b) multi-model ensemble-mean coupled climate model simulations, and (c) multi-model ensemble-mean uncoupled atmospheric model simulations with prescribed observed time varying SSTs. Annual averages are over July to June. All simulation and observational data were interpolated to a common $\sim 2.8^\circ \times 2.8^\circ$ latitude-longitude grid and then truncated to total spherical wavenumber 12 to emphasize subcontinental-scale features (Sardeshmukh and Hoskins 1984).

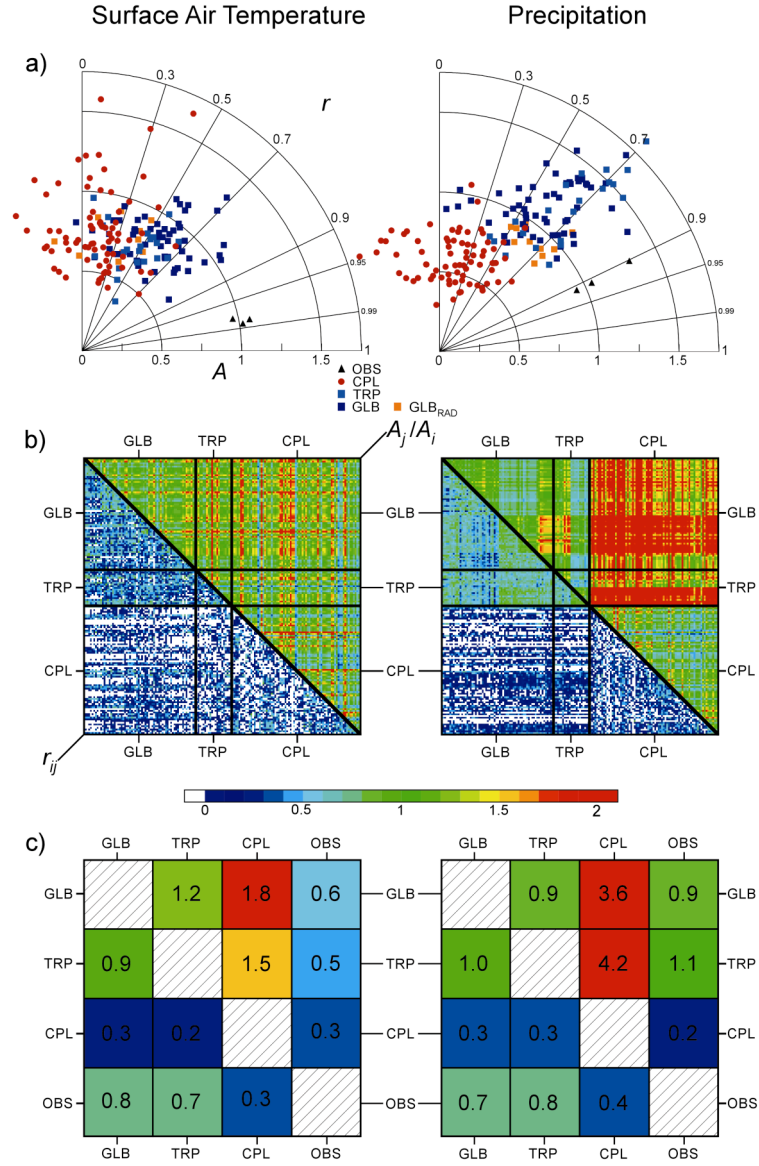


Fig. 2 (a) Taylor diagram comparisons of simulated and observed trends over 1951-1999 of surface air temperature (*left*) and precipitation (*right*) over land areas in the region 20° to 75°N, 170°W to 40°E. Each dot depicts the pattern correlation r (along the angular coordinate) and r.m.s. magnitude ratio A (along the radial coordinate) of a simulated trend field and the observed trend field. Red dots: coupled simulations (CPL); Dark blue squares: uncoupled simulations with prescribed global SST changes (GLB); Orange squares: uncoupled GLB simulations with additional prescribed radiative forcing changes; Light blue squares: uncoupled simulations with SST changes prescribed only in the tropics (TRP). For reference, the temperature and precipitation trend fields obtained from the individual observational datasets (black triangles) are also compared with the average of these observational datasets. (b) Vector Comparison Matrices (VCMs) of the trend vectors from the 76 CPL, 66 GLB, and 21 TRP simulations. The lower left triangle depicts the pattern correlations r_{ij} and the upper right elements depict the r.m.s. magnitude ratio A_j/A_i of each pair i,j among the 163 simulated trend vectors. (c) VCMs of the simulated ensemble-mean and observed trend vectors.

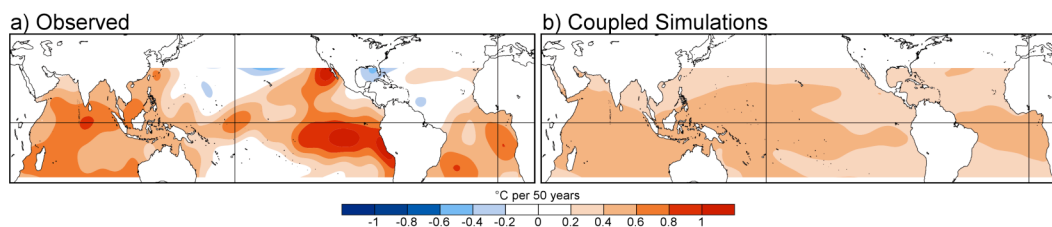


Fig. 3 Trends of annual-mean tropical (30°S - 30°N) SSTs over 1951-1999 derived from (a) observations and (b) the multi-model ensemble-mean of the coupled simulations. All simulation and observational data were interpolated to a common $\sim 2.8^{\circ}\times 2.8^{\circ}$ latitude-longitude grid and then truncated to total spherical wave number 21 to focus on the comparisons of larger scale features (Sardeshmukh and Hoskins 1984).

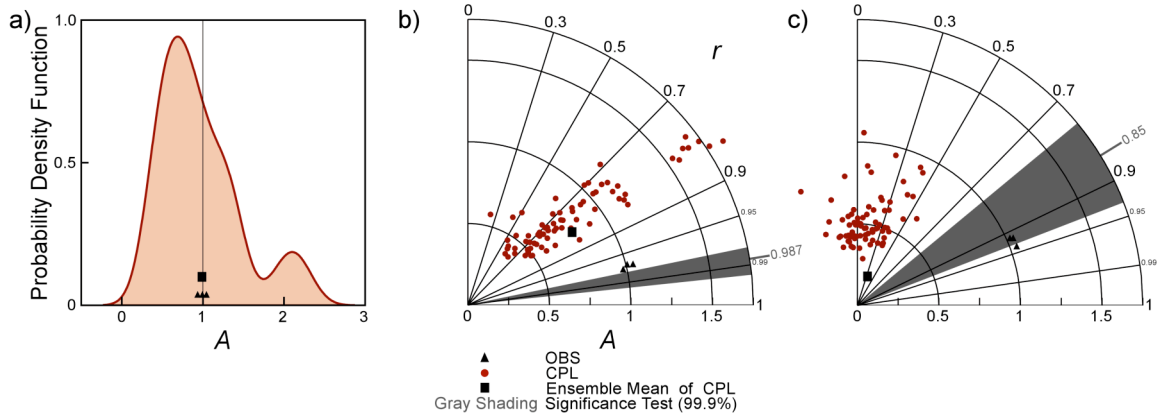


Fig. 4 (a) Estimated probability density function of the magnitude ratio of the 76 area-averaged simulated tropical SST trends with the observed trend. (b) Taylor diagram comparisons of the simulated and observed tropical SST trend fields with their areal means retained. (c) Taylor diagram comparisons of the simulated and observed tropical SST trend fields with their areal means removed. Red dots: coupled simulations (CPL); Black squares: ensemble-mean of coupled simulations. For reference, the trend fields obtained from the individual observational datasets (black triangles) are also compared with the average of these observational datasets. The gray shading in (b, c) indicates 99.9% probability bounds for the observed trend vector to be consistent with the probability distribution of the 76 simulated trend vectors (see text for details).

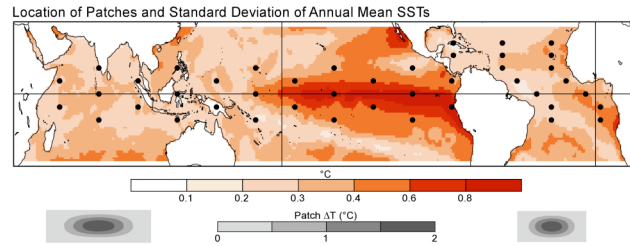


Fig. 5 The location of the SST anomaly patches prescribed in the SST patch experiments. For reference, the standard deviation of annually averaged tropical SSTs from the HadISST dataset (Rayner et al. 2003) during 1951-1999 is also shown. Note that the Indo-Pacific and Atlantic patches are of different sizes. Their full extent is illustrated by the gray-shaded patches at the bottom of figure for the Indo-Pacific (*left*) and Atlantic (*right*) patches.

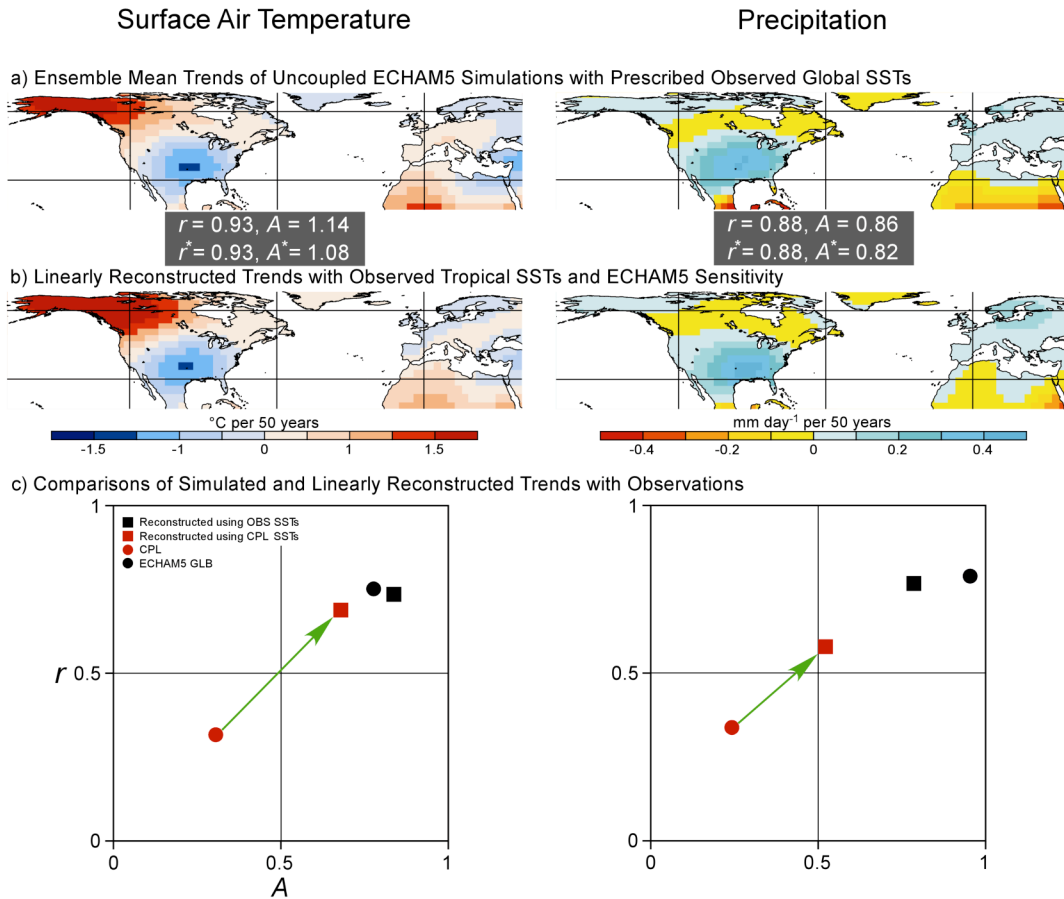


Fig. 6 (a) Trends of annual-mean surface air temperature (*left*) and precipitation (*right*) over 1951-1999 derived from the ensemble-mean uncoupled ECHAM5 simulations with prescribed global SST changes (ECHAM5 GLB; see Table 4). (b) The linearly reconstructed trend response to the observed tropical SST trend over 1951-1999 using a linear response operator G estimated from independent patch experiments. The pattern correlation r and r.m.s. magnitude ratio A of the fields in (a) and (b) with their area means retained, and r^* and A^* with their area means removed, are also shown. (c) Pattern correlation and r.m.s. magnitude ratio with respect to observations of the linearly reconstructed surface air temperature (*left*) and precipitation (*right*) trends over the land areas in (a) and (b). The filled black and red circles show the results for the ensemble-mean trends obtained in the uncoupled ECHAM5 GLB and coupled IPCC/AR4 simulations, and the filled black and red squares show the results for the linearly reconstructed trends obtained using the observed and coupled-model simulated ensemble-mean tropical SST trends. The green arrows indicate the improvement of the trend comparison with observations obtained by removing the effect of the climate biases in the coupled simulations. See text for details. All simulation and observational fields were truncated to total spherical wave number 12 to focus on the comparisons of larger scale features (Sardeshmukh and Hoskins 1984).

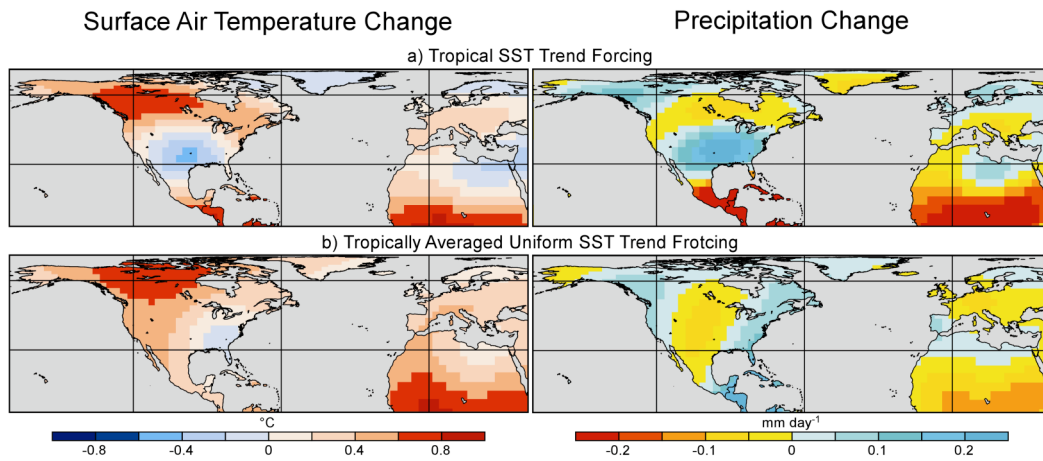


Fig. 7 Annual-mean response of (left) surface air temperature and (right) precipitation (a) to the observed tropical SST trend (TRF; see Fig. 3a), and (b) to its spatially uniform component (TRM). All simulation data were truncated to total spherical wave number 12 to focus on the comparisons of larger scale features (Sardeshmukh and Hoskins 1984).

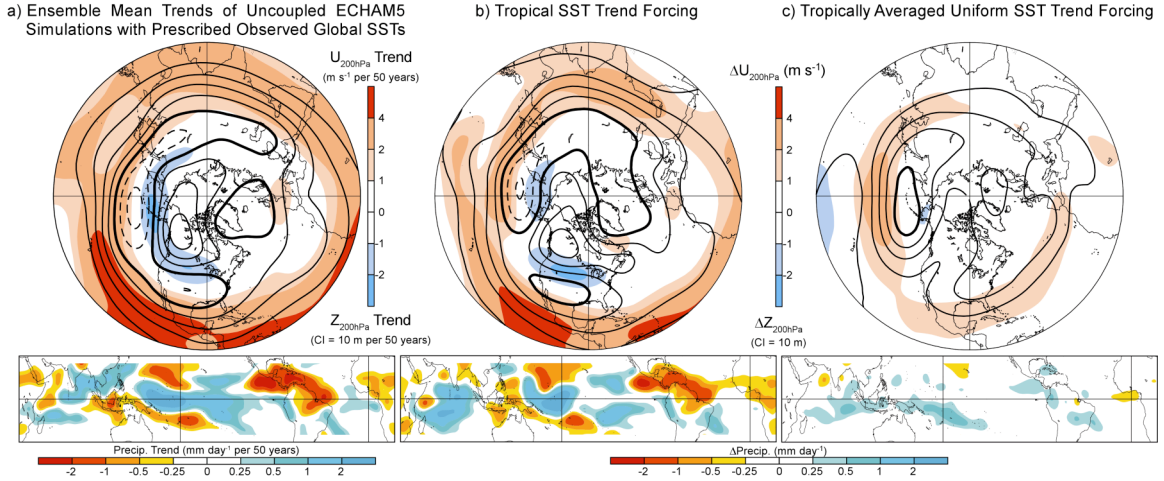


Fig. 8 (a) Trends of annual-mean 200-hPa heights and zonal winds (*top*) and tropical precipitation (*bottom*) over 1951-1999 in the ensemble-mean uncoupled ECHAM5 simulations with prescribed global time-varying SSTs (ECHAM5 GLB). (b-c) Annual-mean response of 200-hPa heights and zonal winds (*top*) and tropical precipitation (*bottom*) to the (b) observed tropical SST trend (TRF, Fig. 3a), and (c) to its spatially uniform component (TRM). The zero contour in the 200-hPa height trend and response fields is thickened and negative contours are dashed.

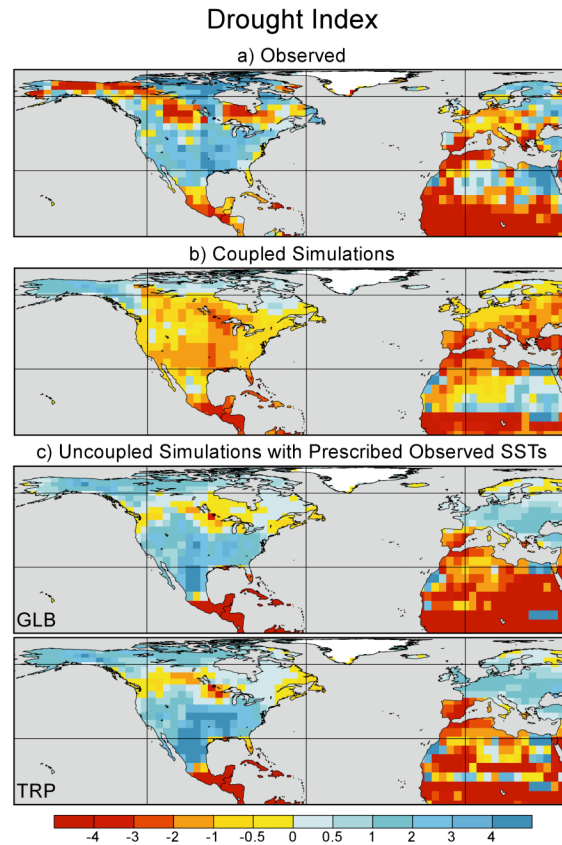


Fig. 9 Trends of annual-mean PDSI in non-glaciated regions over 1951-1999, derived from (a) observations, (b) multi-model ensemble mean of the coupled simulations, and (c) multi-model ensemble mean of the prescribed SST simulations, with the SST changes prescribed globally (GLB) and only in the tropics (TRP). Warm and cold colors (negative and positive values) indicate a trend towards stronger and weaker droughts, respectively, over this period.